Abrupt warming in the latest Permian detected using high-resolution in situ oxygen isotopes of conodont apatite from Abadeh, central Iran

Jun Chen[a,*], Shu-zhong Shen[b], Yi-chun Zhang[c], Lucia Angiolini[d], Mohammad Nabi Gorgij[e], Gaia Crippa[d], Wei Wang[c], Hua Zhang[c], Dong-xun Yuan[c], Xian-hua Li[f], Yi-gang Xu[a]

[a] *State Key Laboratory of Isotope Geochemistry, Guangzhou Institute of Geochemistry, Chinese Academy of Sciences, Guangzhou 510640, China*
[b] *State Key Laboratory for Mineral Deposits Research and School of Earth Sciences and Engineering, Nanjing University, 163 Xianlin Avenue, Nanjing 210023, China*
[c] *State Key Laboratory of Palaeobiology and Stratigraphy, Nanjing Institute of Geology and Palaeontology, Chinese Academy of Sciences, Nanjing 210008, China*
[d] *Dipartimento di Scienze della Terra 'A. Desio', Università degli Studi di Milano, Via Mangiagalli 34, 20133 Milano, Italy*
[e] *Department of Geology, Faculty of Sciences, University of Sistan and Baluchestan, Zahedan, Iran*
[f] *State Key Laboratory of Lithospheric Evolution, Institute of Geology and Geophysics, Chinese Academy of Sciences, Beijing 100029, China*

ARTICLE INFO

ABSTRACT

Climate warming, probably as a result of massive degassing of greenhouse gases from the Siberian Traps magmatism, has often been acclaimed as a major cause of the end-Permian mass extinction. Indeed, several studies have documented a sudden rise in seawater temperatures during the latest Permian-earliest Triassic, as evidenced by oxygen isotopic records measured on conodont apatite. However, whether such a rapid increase in seawater temperatures occurred before, during, or after the mass extinction remains controversial. Moreover, the pattern of this rise in seawater temperatures and its timing relative to the latest Permian-earliest Triassic carbon cycle disruption, mass extinction, as well as the Siberian Traps magmatism still need to be rigorously examined in various regions. In this study, we present high-resolution oxygen isotopic records of conodont apatite ($\delta^{18}O_{apatite}$) from the Upper Permian-lowermost Triassic interval at the Abadeh section, central Iran that are analyzed with in situ secondary ion mass spectrometry (SIMS) method. The $\delta^{18}O_{apatite}$ results from Abadeh demonstrate a clear pattern consisting of three phases: **(1)** From the lower Wuchiapingian *Clarkina dukouensis* Zone to the end-Permian mass extinction horizon, $\delta^{18}O_{apatite}$ values are relatively stable, fluctuating in the range of 18.28-20.15‰ with an average of 19.44‰. **(2)** $\delta^{18}O_{apatite}$ value remains high as 19.26‰ at the mass extinction horizon. Above this horizon, a sudden decrease occurs in the *Clarkina hauschkei* Zone and reaches a low value of 17.05‰ close to the Permian-Triassic boundary. **(3)** In the lowermost Triassic, $\delta^{18}O_{apatite}$ values maintain a low baseline in the range of 16.92-17.39‰ with an average of 17.11‰. Overall, the most dramatic change in $\delta^{18}O_{apatite}$ values (i.e., a decrease of ~2‰), converting into an abrupt warming of ~10 °C, occurred above the mass extinction horizon and below the Permian-Triassic boundary at Abadeh. The Abadeh $\delta^{18}O_{apatite}$ record is consistent with previous results documented in South China, Iran, and Armenia in terms of the timing and magnitude of a substantial warming, and therefore represents a global signature. If applying the high-precision temporal framework established in the well-dated Meishan GSSP section to Abadeh, the abrupt warming of ~10 °C took only a maximum duration of ~37 kyr (thousand years). By projecting the carbon cycle change, temperature rise, mass extinction at the Abadeh and Meishan sections, and the temporal evolution of the Siberian Traps magmatism onto a unified timescale, the temporal correlation strongly suggests that the switch from dominantly extrusive eruptions to widespread sill intrusions is probably the most annihilating phase of the Siberian Traps magmatism, and is temporally consistent with the end-Permian mass extinction.

* Corresponding author at: State Key Laboratory of Isotope Geochemistry, Guangzhou Institute of Geochemistry, Chinese Academy of Sciences, 511 Kehua Street, Wushan, Tianhe District, Guangzhou 510640, China.

E-mail addresses: junchen@gig.ac.cn (J. Chen), szshen@nju.edu.cn (S.-z. Shen), yczhang@nigpas.ac.cn (Y.-c. Zhang), lucia.angiolini@unimi.it (L. Angiolini), mngorgij@science.usb.ac.ir (M.N. Gorgij), gaia.crippa@unimi.it (G. Crippa), weiwang@nigpas.ac.cn (W. Wang), hzhang@nigpas.ac.cn (H. Zhang), dxyuan@nigpas.ac.cn (D.-x. Yuan), lixh@gig.ac.cn (X.-h. Li), yigangxu@gig.ac.cn (Y.-g. Xu).

1. Introduction

The broad temporal correlation between large igneous provinces (LIPs) and mass extinctions (e.g., Rampino and Stothers, 1988; Wignall, 2001; Courtillot and Renne, 2003; Ganino and Arndt, 2009; Bond and Wignall, 2014; Bond and Grasby, 2017; Ernst and Youbi, 2017) has often been invoked to explain catastrophic biodiversity decline in Earth history, most notably as in the associated events of the Siberian Traps magmatism and the end-Permian mass extinction (EPME) (Renne and Basu, 1991; Renne et al., 1995; Reichow et al., 2009; Saunders and Reichow, 2009; Svensen et al., 2009; Algeo et al., 2011; Svensen et al., 2018; Shen et al., 2019a; Wang et al., 2019). However, significant improvements in high-precision U-Pb geochronology from the Meishan GSSP (Global Stratotype Section and Point) section suggested that the maximum duration of abrupt biodiversity decline around the Permian-Triassic boundary (PTB) (Beds 25-28; i.e., maximum extinction interval) was only 61 ± 48 kyr (thousand years) (Burgess et al., 2014). More recently, a comprehensive study from a highly expanded PTB section at Penglaitan, Guangxi, South China (Shen et al., 2019b) indicated a nearly instantaneous biotic crisis that is coincident with the EPME at Meishan (i.e., Bed 25), and was limited to $< 31 \pm 31$ kyr. As for the Siberian Traps magmatism, it most likely lasted for over ~1 Myr (million years) (Burgess and Bowring, 2015).

Such disparity suggests that the cause-and-effect connection between the Siberian Traps magmatism and the EPME might not be as simple as previously thought. Although a causal connection is permitted on the basis that the Siberian Traps magmatism occurred prior to, during, and after the EPME (Burgess and Bowring, 2015), whether one or more pulses of magmatism drove a drastic deterioration in global environmental conditions and ultimately led to rapid collapse of ecosystems (Shen et al., 2011, 2019b; Burgess et al., 2014) awaits further assessment. Precise timing and duration of such pulses of magmatism are difficult to determine even with high-precision geochronology (Burgess and Bowring, 2015). Additional means such as near-continuous, high-resolution palaeoenvironmental and palaeoclimatic proxies (Chen and Xu, 2019) are useful in enhancing temporal constraints. Gas production from major LIPs such as the Siberian Traps potentially can affect the Earth's climate at many timescales (Robock, 2000), among which SO_2, H_2S and sulfate aerosols could cause short-term cooling, and greenhouse gases (CO_2, CH_4) could lead to long-term warming. On the other hand, silicate and carbonate weathering consumes atmospheric CO_2, thus there is essentially a tug of war between degassing and weathering and the outcome primarily controls climate (Dessert et al., 2003; Grard et al., 2005; Saltzman, 2017; Johansson et al., 2018). High-resolution palaeotemperature records, integrated with other lines of evidence such as carbon cycle change and continental weathering, can be pivotal in examining the causal-and-effect link between LIP magmatism, environmental deterioration and biotic crisis.

In this study, we investigated the Upper Permian-lowermost Triassic interval at the Abadeh section, central Iran. Oxygen isotopic compositions of conodont apatite ($\delta^{18}O_{apatite}$) are analyzed with in situ secondary ion mass spectrometry (SIMS) method, and subsequently a high-resolution seawater temperature profile is reconstructed. Comparisons are made with previously documented records from various regions to verify whether some distinct signatures are global in nature. Lastly, we evaluate the potential links between the Siberian Traps magmatism (including explosive, effusive and intrusive phases), environmental changes, and end-Permian mass extinction.

2. Geological setting and biostratigraphic framework

Palaeogeographic reconstructions (Muttoni and Kent, 2019) suggested that the Abadeh region was situated on the northern shore of the Neotethys, in the Sanandaj–Sirjan zone belonging to the Cimmerian terranes (Hassanzadeh and Wernicke, 2016). The investigated

stratigraphic succession (PTB coordinates: 30°53′43.76″N, 53°12′16.16″E) is located at the Hambast Valley, about 60 km SE of the Abadeh town in central Iran (Fig. 1). The Permian-Triassic sequence is well exposed in this area and has been extensively studied for decades (Taraz, 1969, 1971, 1973, 1974; Taraz et al., 1981; Heydari et al., 2000, 2003; Korte et al., 2004; Kozur, 2004, 2005; Horacek et al., 2007; Richoz et al., 2010; Liu et al., 2013). In a comprehensive, historical report by the Iranian-Japanese Research Group (Taraz et al., 1981), the results of a detailed palaeontological and sedimentological study were presented, with a general scheme of litho- and chronostratigraphic subdivision that is widely used ever since.

Overall, seven lithological units (Units 1-7) of Permian age and five units (Units a-e) of roughly Triassic age have been identified at the Abadeh section. Units 1, 2, and 3 are distinguished in the Surmaq Formation, which has a total thickness of about 550 m (Taraz et al., 1981) and is composed of dark thick-bedded limestone containing extremely abundant fusulinids including *Eopolydiexodina* in the lower, *Veeberkina* in the middle and *Chusenella abichi* in the upper part of the formation (Shen et al., 2009). The overlying Abadeh Formation consists of two units: Unit 4 and Unit 5. Unit 4 is about 400 m thick (Taraz et al., 1981; Heydari et al., 2000) and is dominated by bioclastic limestone alternated with mudstone and calcareous mudstone and contains abundant benthic fossils such as foraminifers, bryozoans, crinoids and brachiopods (Shen et al., 2009). The upper part of Unit 4 is mainly composed of black shale with thin limestone interbeds (Taraz et al., 1981), which are a little more prominent in the middle part where they are accompanied by discontinuous chert layers or nodules that are distinct and can be used to trace those beds in the field (e.g., B-13 in Fig. 2A). Unit 4 grades upward into Unit 5 (-77.6 to -36.7 m; Fig. 3), which is dominated by dark thick-bedded bioclastic limestone (Fig. 2B) containing abundant foraminifers and the fusulinid *Codonofusiella-Reichelina* fauna (Shen et al., 2009). Unit 6 (-36.7 to -15.5 m; Fig. 3) of the Hambast Formation consists of mudstone alternated with thin-medium bedded bioclastic limestone. The lower part of this unit contains abundant well-preserved brachiopods, for which it is often called the "*Araxilevis* Bed". Unit 7 (-15.5 to -1.5 m) of the Hambast Formation is mainly composed of reddish thin-bedded nodular limestone containing abundant ammonoids and conodonts. The topmost ~4 m of this unit contains abundant *Paratirolites* and therefore is usually referred as the "*Paratirolites* Bed" (Taraz et al., 1981; Ghaderi et al., 2014b; Leda et al., 2014; Korn et al., 2016). The Hambast Formation is overlain by the Elikah Formation, which is easily distinguished from the underlying reddish limestone by its overall dark color, very-thin-bedded coarse limestone (Fig. 2C). The basal part of the Elikah Formation, with a total thickness of ~1.5 m, contains a distinct fan-like "Microbialite Bed" and the "Boundary Clay" located at the very base (Shen et al., 2009; Angiolini et al., 2017).

Although the whole Permian sequence in the Hambast Valley was investigated during the field trips in 2009 and 2017 (Shen et al., 2009; Angiolini et al., 2017), this study focused on the Upper Permian (Lopingian)-lowermost Triassic interval, which ranges from the upper part of Unit 5 (Abadeh Formation), the complete Unit 6 and Unit 7 (Hambast Formation), to the lower part of Unit a (Elikah Formation) (Figs. 2, 3). High-resolution stratigraphic correlations of the Lopingian succession between Iran and South China have been presented in recent studies, mainly based on conodont biostratigraphy and carbon, strontium isotopic chemostratigraphy (Shen and Mei, 2010; Liu et al., 2013; Shen et al., 2013; Gliwa et al., 2020). At the Abadeh section, the Guadalupian-Lopingian boundary (GLB) was tentatively placed at -46.5 m of the upper part of Unit 5, which is characterized by the transition from conodont species *Jinogondolella postbitteri* to *Clarkina dukouensis* (Shen and Mei, 2010), and a negative shift of $\delta^{13}C_{carb}$ (~2‰) above the lowest $^{87}Sr/^{86}Sr$ value of 0.7069-0.7070 (Liu et al., 2013). The Wuchiapingian-Changhsingian boundary (WCB) was suggested to be at -14.5 m, supported by the conodont zones of *Clarkina orientalis* (uppermost Wuchiapingian) and *C. wangi* (lowermost Changhsingian)
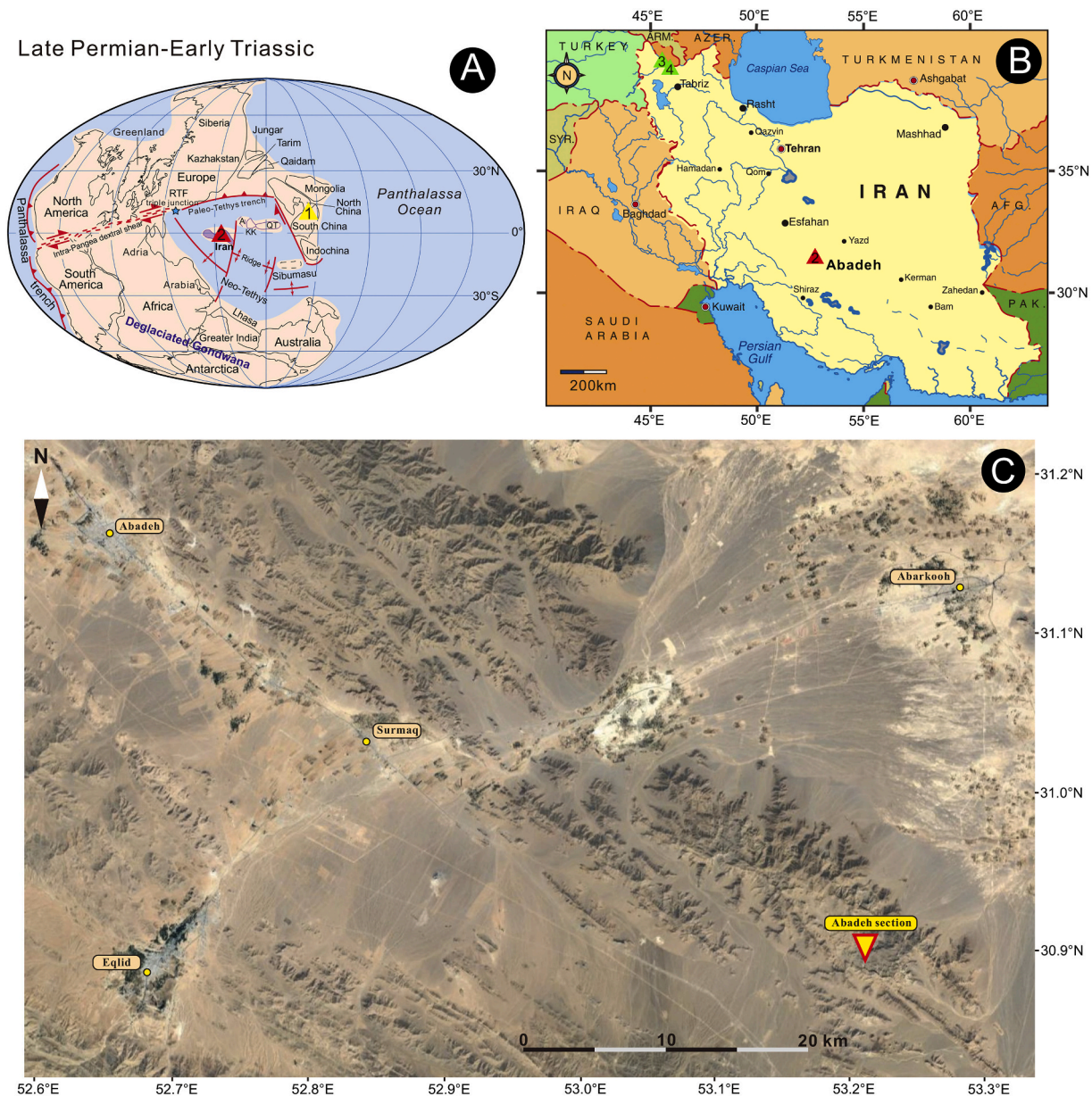
Fig. 1. (A) Palaeogeographic reconstruction of the Late Permian-Early Triassic (Muttoni and Kent, 2019) showing the Meishan (1) and Abadeh (2) sections. **(B)** Geographic map showing the position of the Abadeh section (2) in central Iran and Kuh-e-Ali Bashi (3) and Zal sections in NW Iran, modified from Shen and Mei (2010). **(C)** Google Earth image showing the Permian-Triassic boundary (PTB) section at Abadeh (30°53′43.76″N, 53°12′16.16″E), located in the Hambast Valley, about 60 km SE of the Abadeh town in central Iran.

(Shen and Mei, 2010; Shen et al., 2013), in addition to a minor negative shift of $\delta^{13}C_{carb}$ (~1.3‰) and $^{87}Sr/^{86}Sr$ value of 0.7071–0.7072 (Liu et al., 2013).

The PTB interval that spans the Hambast-Elikah formations is of great importance and has been repeatedly studied by various groups in recent years (Korte et al., 2004; Kozur, 2004, 2005, 2007; Horacek et al., 2007; Richoz et al., 2010; Liu et al., 2013; Shen et al., 2013; Shooshtarizadeh and Yazdi, 2013; Ghaderi et al., 2014b; Leda et al., 2014). It can be subdivided into four distinct units, in ascending order: (1) "*Paratirolites* Bed" (-5.15 to -1.50 m), which is a reddish micritic limestone unit containing abundant ammonoids that can be well correlated in the Transcaucasia, northwestern and central Iran; (2) "Boundary Clay" (-1.50 to -1.40 m), which is a thin, pale silty marl that marks a sharp but continuous transition into the Elikah Formation and represents the mass extinction horizon; (3) "Microbialite Bed" (-1.40 to 0 m), which contains three levels of branching microbial structures

(Fig. 2C) and was referred as "stromatolite beds" (Taraz et al., 1981), "synsedimentary carbonate cement layer" (Heydari et al., 2003), "stromatolites (thrombolites)" (Kozur, 2005, 2007), or "microbial limestone" (Richoz et al., 2010); and (4) thin-bedded limestone (0 to ~10 m), which is finely laminated, dark in color, and forms a small cliff that can be easily traced in the field. In contrast to the mass extinction horizon that is widely accepted to place at the top of "*Paratirolites* Bed" (i.e., the base of "Boundary Clay"), the position of the PTB at Abadeh is contradictory in different studies. It was originally placed at the boundary between Unit 7 and Unit a (Taraz et al., 1981). Later, the index fossil *Hindeodus parvus* was found at 1.38 m above the base of "Boundary Clay" (Korte et al., 2004; Kozur, 2005) or 25-30 cm above the "boundary shale" (Horacek et al., 2007; Richoz et al., 2010), which are either close to the top or the base of "Microbialite Bed". A worldwide survey on the stratigraphic distribution of PTB microbialites (Kershaw et al., 2012) indicated that the biostratigraphic boundary is
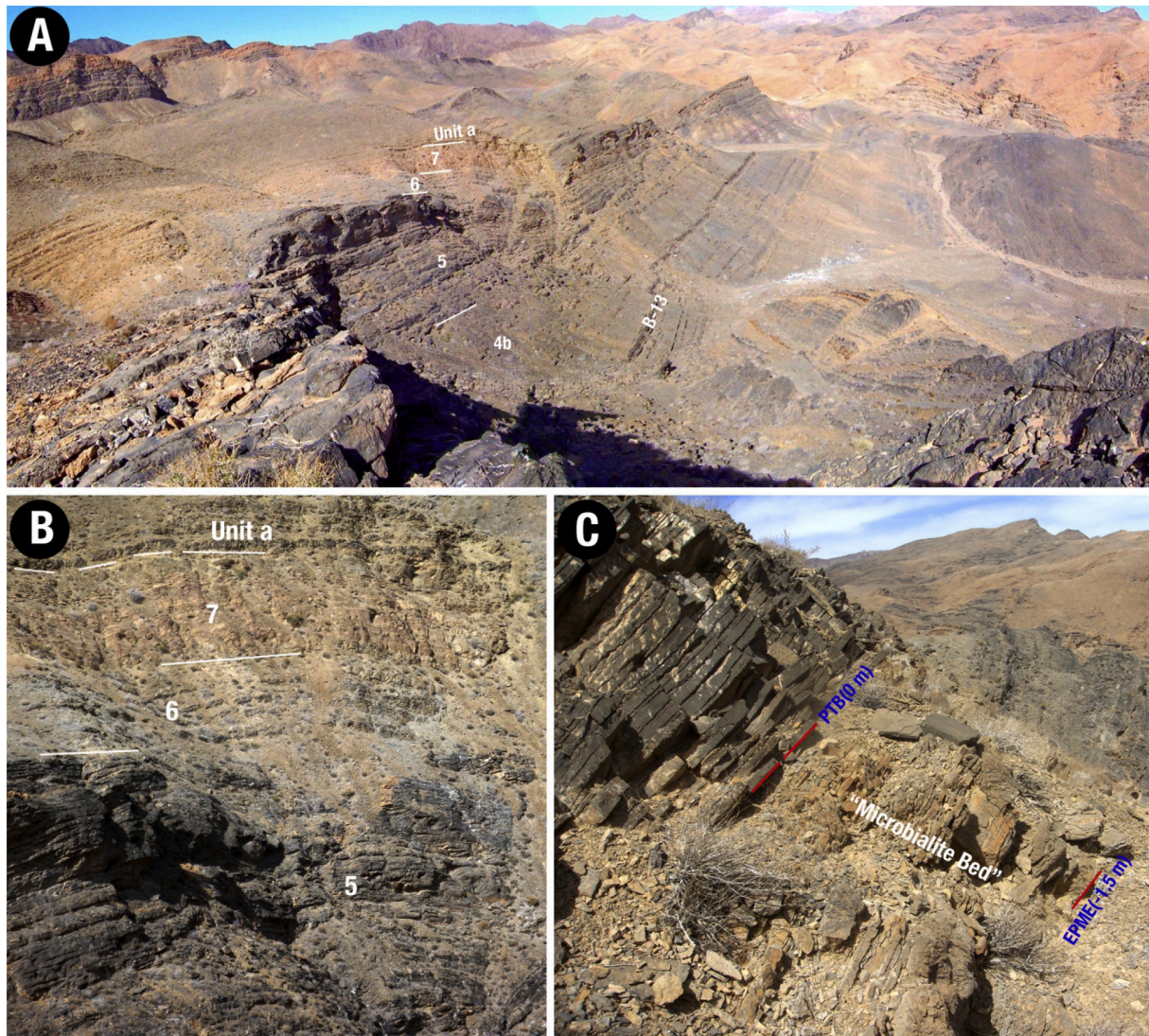
Fig. 2. Field photos showing **(A)** the panoramic view of the Upper Permian and lowermost Triassic sequence at Abadeh, **(B)** the investigated interval of this study, ranging from the upper part of Unit 5 (Abadeh Formation, Permian) to the lower part of Unit a (Elikah Formation, Triassic), and **(C)** the Permian-Triassic boundary (PTB) interval of the Abadeh section.

most likely close to the top of microbialite bed. Conodonts recovered from our samples are not abundant enough to allow us applying the "sample-population" approach that could potentially identify the lineage of *Hindeodus praeparvus – H. parvus – H. postparvus* and define the PTB with confidence (Chen et al., 2009), therefore, we chose a more conservative option, that is placing the PTB at the base of thin-bedded limestone (Fig. 2C; 0 m, i.e., at the top of the "Microbialite Bed").

In summary, the constraining data for the Abadeh section, including the positions and ages of the GLB (Zhong et al., 2014), WCB (Jin et al., 2006; Shen et al., 2011), end-Permian mass extinction (Burgess et al., 2014), and PTB (Burgess et al., 2014), are listed in **Table 1**. Calculated sediment accumulation rates and ranges of conodont zones are also presented (**Table 1**).

3. Materials and methods

A total of 90 bulk rock samples were collected from the 60-m interval around the PTB (Fig. 3), of which 72 were productive after having been processed in the lab at the Nanjing Institute of Geology and Palaeontology, Chinese Academy of Sciences, following standard procedures. CAI (Color Alteration Index) values of conodont apatite from the Abadeh section are in the range of 1.5-2.0, suggesting minimal thermal alteration during burial. During sample preparation, specimens with anomalous color (indicative of potential thermal alteration) and coarse recrystallized surface (indicative of potential diagenetic overprint) were strictly avoided. Following this standard, a total of 185 conodont specimens from 72 samples (*Clarkina* sp., *Hindeodus* sp., and ramiforms recovered from same horizon are treated as different samples; Supplementary **Table S1**) were selected for analyses of oxygen isotopes, which covered the interval from the lower Wuchiapingian *Clarkina dukouensis* Zone to the lowermost Triassic *Isarcicella isarcica* Zone (Fig. 3).

We used SIMS method to measure oxygen isotopic compositions of conodont apatite ($\delta^{18}O_{apatite}$) from the Abadeh section, with a Cameca IMS-1280 at the CA-SIMS Laboratory of the Institute of Geology and Geophysics, Chinese Academy of Sciences. Analytical methods, including sample mount preparation, polishing, reflected light imaging, coating, and in situ measurement, following the standard analytical procedures of the SIMS laboratory as described in Chen et al. (2016) and Shen et al. (2019b). Measured $^{18}O/^{16}O$ was normalized using the Vienna Standard Mean Ocean Water compositions (VSMOW; $^{18}O/^{16}O$ = 0.0020052), and then corrected for the instrumental mass
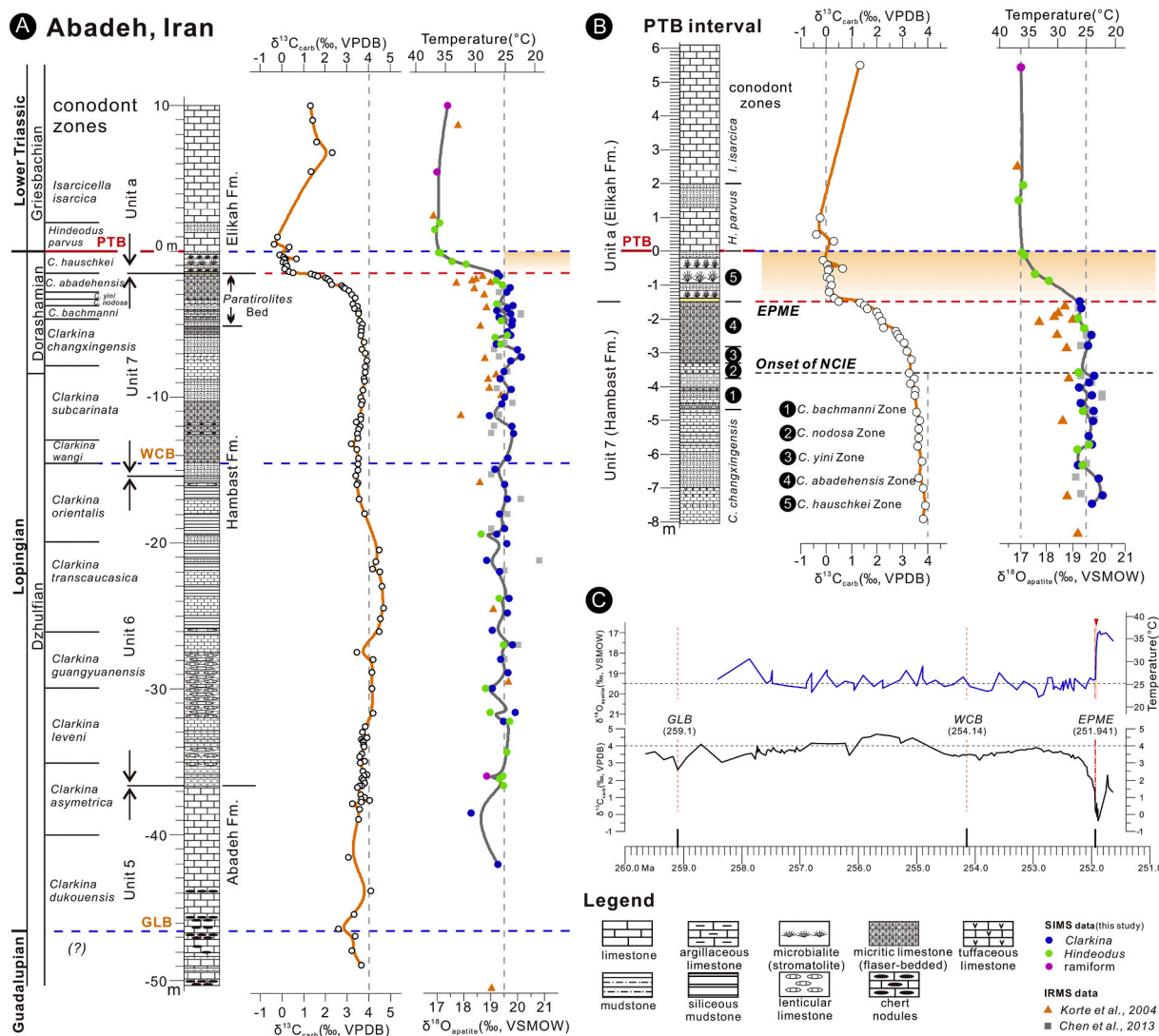
Fig. 3. Whole rock carbonate carbon isotope ($\delta^{13}C_{carb}$) record (Liu et al., 2013), conodont apatite oxygen isotope ($\delta^{18}O_{apatite}$) profile and calculated relative seawater temperatures from the Abadeh section. Lithology, conodont biostratigraphy (Shen and Mei, 2010), and biostratigraphic boundaries of GLB (Guadalupian-Lopingian boundary), WCB (Wuchiapingian-Changhsingian boundary), and PTB (Permian-Triassic boundary) are provided. **(A)** Full record of the investigated interval, scaled to the thickness of strata; **(B)** Close-up of PTB interval, scaled to the thickness of strata; **(C)** Full $\delta^{13}C_{carb}$ and $\delta^{18}O_{apatite}$ profiles scaled to absolute ages, after a temporal framework is established (Table 1).

fractionation factor (IMF). The IMF was corrected (Li et al., 2010a; Li et al., 2010b) using the Durango apatite standard of the CA-SIMS Laboratory (Chen et al., 2016; Shen et al., 2019b). Durango apatite was used as a primary reference material (RM), and Qinghu apatite was measured as a secondary laboratory reference to monitor external precision. $\delta^{18}O_{apatite}$ values of randomly selected Durango crystals have been independently determined at the GeoZentrum Nordbayern, Universität Erlangen-Nürnberg using the conventional isotope ratio mass spectrometry (IRMS) method (Joachimski et al., 2009). Analyses were calibrated by measuring standards TU1 and TU2 as 21.11‰ and 5.45‰, respectively (Vennemann et al., 2002). With this calibration, reference standard NBS 120c was measured as 21.8 ± 0.17‰ (1σ, n = 10), and our Durango apatite gave a mean $\delta^{18}O$ value of 8.8 ± 0.04‰ (1σ, n = 10) (Chen et al., 2016). During four consecutive analytical sessions from June 13 to June 17, 2014, a total of 648 analyses were run for the Abadeh conodont apatite (Table 2; Supplementary Table S1). The reproducibility (1σ) of measured conodont samples ranges from 0.03 to 0.35‰, with an average of 0.26‰ (n = 72). For primary Durango standard, the reproducibility is 0.19‰ (1σ, n = 232). As for the paired in-house Qinghu apatite, the 4-day monitoring process yields

a weighted mean of $\delta^{18}O$ = 4.62 ± 0.27‰ (1σ, n = 99), which is within uncertainty of the long-term average of 4.46‰ (Chen et al., 2016) (Supplementary **Table S2**).

4. Results

Our $\delta^{18}O_{apatite}$ data from the Abadeh section clearly shows a three-phase pattern (**Fig. 3**). From the lower Wuchiapingian *Clarkina dukouensis* Zone (-42.05 m; lowest data point of this study) to the mass extinction horizon (-1.50 m; defined at the base of "Boundary Clay"), $\delta^{18}O_{apatite}$ values fluctuate in the range of 18.28-20.15‰ with an average of 19.44‰ (n = 64), which are highly stable with only rare data higher than 20‰ (n = 2) and lower than 19‰ (n = 7). $\delta^{18}O_{apatite}$ value remains high as 19.26‰ at the mass extinction horizon. Above this horizon, a sudden decrease occurs in the *Clarkina hauschkei* Zone and reaches a value of 17.05‰ close to the PTB (-0.06 m) and the lowest value of 16.92‰ at 1.50 m of the *Hindeodus parvus* Zone (Table 2). In the lowermost Triassic, $\delta^{18}O_{apatite}$ values maintain a low baseline in the range of 16.92-17.39‰ with an average of 17.11‰ (n = 4). Assuming the $\delta^{18}O_{seawater}$ value is constant at -1‰ (VSMOW) in

Table 1

Established temporal framework at the Abadeh section, including key constraining data (Shen et al., 2011; Burgess et al., 2014; Zhong et al., 2014), calculated accumulation rates, and range of conodont zones (Shen and Mei, 2010; this study).

Depth(m)	Position	Age(Ma)
a) Constraining data		
0	PTB (FAD of *H. parvus*)	251.902
-1.50	Mass extinction level (base of "Boundary Clay")	251.941
-14.5	WCB	254.14
-46.5	GLB	259.10

#	Interval	Accumulation rate(cm/kyr)
b) Sediment accumulation rates		
1	0.00 - top of section	3.8461538
2	-1.50 - 0	3.8461538
3	-14.5 - -1.50	0.5911778
4	-46.5 - -14.5	0.6451613
5	base of section - -46.5	0.6451613

#	Conodont zone	Range
c) Range of conodont zones		
1	*I. isarcica*	2.00 - unconstrained
2	*H. parvus*	0.00 - 2.00
3	*C. hauschkei*	-1.50 - 0
4	*C. abadehensis*	-2.8 - -1.50
5	*C. yini*	-3.3 - -2.8
6	*C. nodosa*	-3.75 - -3.3
7	*C. bachmanni*	-4.7 - -3.75
8	*C. changxingensis*	-7.8 - -4.7
9	*C. subcarinata*	-13.0 - -7.8
10	*C. wangi*	-14.5 - -13.0
11	*C. orientails*	-20.0 - -14.5
12	*C. transcaucasica*	-26.0 - -20.0
13	*C. guangyuanensis*	-30.0 - -26.0
14	*C. leveni*	-35.0 - -30.0
15	*C. asymmetrica*	-40.0 - -35.0
16	*C. dukouensis*	-46.5 - -40.0
17	*C. postbitteri* (?)	? - -46.5

the Late Permian-earliest Triassic "ice-free" world, calculations of paleotemperature using a recently proposed phosphate–water temperature scale (Lécuyer et al., 2013) suggest that the seawater temperatures remain stable around 25.5 °C below and at the mass extinction horizon; a sudden and substantial rise occurs above the mass extinction horizon, from 26.2 °C at the mass extinction horizon (-1.50 m) to 31.5 °C at -0.88 m, 36.2 °C close to the PTB (-0.06 m), and reaches the peak of our dataset at 36.8 °C (1.5 m) (Table 2;Fig. 3).

5. Discussions

5.1. Climate warming in the latest Permian as a global signature

$\delta^{18}O_{apatite}$ data from the Abadeh section have been reported in two previous studies (Korte et al., 2004; Chen et al., 2013), both of which used the conventional IRMS method. A comparable stratigraphic interval similar to this study was documented by Korte et al. (2004). However, the change in seawater temperatures across the extinction horizon was not emphasized (Korte et al., 2004), probably due to limited samples around the EPME, and some questionable measurements below the extinction horizon that were nearly identical as those above (Figs. 3, 4). A total of 33 samples from the Abadeh section, which belong to the same collection that is used in this study, were measured by Chen et al. (2013) (Figs. 3, 4). Since the IRMS technique requires large sample size (> 0.5 mg) and conodonts around the EPME interval are usually small in size and low in abundance, $\delta^{18}O_{apatite}$ data above the mass extinction horizon were not available in Chen et al. (2013) (Figs. 3, 4). Therefore, both studies using the IRMS method (Korte

et al., 2004; Chen et al., 2013) have not convincingly shown substantial changes in seawater temperature in the Upper Permian-lowermost Triassic. In situ SIMS method enables multiple measurements on individual conodont elements, therefore is more suitable for high-resolution reconstruction of seawater temperatures around the EPME (Chen et al., 2016; Shen et al., 2019b). A compilation of SIMS and IRMS data (Figs. 3, 4) shows that our SIMS dataset confirmed the overall long-term trend of the IRMS dataset. However, it also indicates that there are likely some anomalous IRMS data points from Korte et al. (2004) and Chen et al. (2013).

The Abadeh section in central Iran can be well correlated with the NW Iranian sections such as Kuh-e-Ali Bashi and Zal in terms of lithostratigraphy (Ghaderi et al., 2014a; Leda et al., 2014), conodont biostratigraphy (Shen and Mei, 2010; Shooshtarizadeh and Yazdi, 2013; Ghaderi et al., 2014b), and chemostratigraphy (Horacek et al., 2007; Korte and Kozur, 2010; Richoz et al., 2010; Shen et al., 2013). Despite several abnormal data points (e.g., AB -100, AB +124 from Kuh-e-Ali Bashi, and ZL -65, ZL +415 from Zal) that probably can be excluded as they are too high or too low comparing to adjacent data points, the IRMS-based $\delta^{18}O_{apatite}$ profiles from NW Iran (Schobben et al., 2014) are highly comparable with our SIMS data from Abadeh (Fig. 4), such as the limited variations around an average value of ~19.5‰ below and at the extinction horizon, and a sudden decrease to ~17.0‰ above the extinction horizon. Therefore, it is fair to conclude that the seawater temperature changes in central and NW Iran are synchronous; most importantly, the sudden rise above the mass extinction horizon in both regions are nearly identical in timing and magnitude.

More recently, Joachimski et al. (2020) reported conodont biostratigraphy, carbon isotopes of carbonates ($\delta^{13}C_{carb}$), and IRMS-based oxygen isotopes of conodont apatite ($\delta^{18}O_{apatite}$) from two Permian-Triassic sections (Chanakhchi and Vedi II) in SW Armenia, which are located only less than 150 km NW of the Kuh-e-Ali Bashi section, Iran. The Armenian records (Joachimski et al., 2020), especially the $\delta^{18}O_{apatite}$ profile of the Chanakhchi section, is similar to those of the Kuh-e-Ali Bashi and Zal sections in NW Iran (Schobben et al., 2014) and the Abadeh section in central Iran (Korte et al., 2004; Chen et al., 2013; this study), in terms of limited variations in most of the Lopingian and a substantial decrease in the uppermost Permian. However, a slight difference does exist. The abrupt decrease in $\delta^{18}O_{apatite}$ at the Chanakhchi section is confined to a 17-cm interval, starting from 19.54‰ at the very top of the reddish nodular limestone ("*Paratirolites* Bed"; Akhura Formation) to 17.10‰ within the reddish marl ("Boundary Clay") and below the "Microbialite Bed". In contrast, based on our high-resolution SIMS data from Abadeh as an example, $\delta^{18}O_{apatite}$ value remains as high as 19.26‰ in the "Boundary Clay" (i.e., the mass extinction horizon), and the decrease to 17.05‰ occurs throughout the 1.4-m interval of the "Microbialite Bed" (Figs. 2, 3). In addition to such obvious discrepancy with respect to oxygen isotope values and corresponding lithological units (i.e., "*Paratirolites* Bed", "Boundary Clay", and "Microbialite Bed"), conodont biostratigraphy also casts doubt on synchronicity between the Armenian and Iranian records. The abrupt decrease in $\delta^{18}O_{apatite}$ and thus a rapid climate warming at the Chanakhchi section is located in the *Clarkina iranica* (= *C. abadehensis*; Shen and Mei, 2010) and *C. hauschkei* zones, whereas in Abadeh as well as other sections in Iran, it occurs in the *C. hauschkei* Zone (Schobben et al., 2014; this study).

In the South China region, a number of Permian-Triassic sections have been studied for oxygen isotopes of conodont apatite with conventional IRMS method as well as high-resolution SIMS technique, such as the Meishan GSSP (Joachimski et al., 2012; Sun et al., 2012; Chen et al., 2013, 2016), Shangsi (Joachimski et al., 2012; Sun et al., 2012; Chen et al., 2016), Bianyang (Jiang et al., 2015), Liangfengya (Chen et al., 2016), Daijiagou (Chen et al., 2016), Penglaitan (Shen et al., 2019b), and Xikou (Wang et al., 2020) sections. A substantial decrease in $\delta^{18}O_{apatite}$ (i.e., rise in seawater temperatures) during the latest Permian has been identified in all of the seven studied sections. Since

Table 2
In situ oxygen isotopic compositions of conodont apatite ($\delta^{18}O_{apatite}$) from the Abadeh section.

#	Sample	Stage	Conodont zone	Depth	Age	Type[1]	$\delta^{18}O_{apatite}$	sd[2]	n	se[3]	T(°C)[4]
Ab-1	TEH-(10m)	Induan	*I. isarcica*	10.00	251.6420	R	17.39	0.35	5	0.16	34.63
Ab-2	TEH-(5.45m)	Induan	*I. isarcica*	5.45	251.7603	R	17.01	0.22	4	0.11	36.36
Ab-3	TEH-(1.9 ~ 2.0m)	Induan	*H. parvus*	1.95	251.8513	H	17.10	0.32	8	0.11	35.96
Ab-4	TEH-(1.5m)	Induan	*H. parvus*	1.50	251.8630	H	16.92	0.22	8	0.08	36.75
Ab-5	TEH-(-0.06m)	Changhsingian	*C. hauschkei*	-0.06	251.9036	H	17.05	0.24	11	0.07	36.16
Ab-6	TEH-(-0.1 ~ -0.15m)	Changhsingian	*C. hauschkei*	-0.12	251.9051	H	17.15	0.26	10	0.08	35.73
Ab-7	TEH-(-0.65 ~ -0.7m)	Changhsingian	*C. hauschkei*	-0.68	251.9197	H	17.55	0.24	7	0.09	33.91
Ab-8	TEH-(-0.85 ~ -0.9m)	Changhsingian	*C. hauschkei*	-0.88	251.9249	H	18.09	0.28	12	0.08	31.51
Ab-9	TEH-(-1.5m)	Changhsingian	*C. hauschkei*	-1.50	251.9410	C	19.26	0.27	4	0.13	26.24
Ab-10	TEH-(-1.7m)	Changhsingian	*C. abadehensis*	-1.70	251.9748	C	19.32	0.33	17	0.08	25.94
Ab-11	TEH-(-2m)	Changhsingian	*C. abadehensis*	-2.00	252.0256	H	19.21	0.25	9	0.08	26.47
Ab-12	TEH-(-2.3m)	Changhsingian	*C. abadehensis*	-2.30	252.0763	H	19.45	0.14	3	0.08	25.39
Ab-13	TEH-(-2.5m)	Changhsingian	*C. abadehensis*	-2.50	252.1102	C	19.72	0.20	13	0.05	24.14
Ab-14	TEH-(-2.8m)	Changhsingian	*C. abadehensis*	-2.80	252.1609	C	19.60	0.30	13	0.08	24.70
Ab-15	TEH-(-3.6m)	Changhsingian	*C. nodosa*	-3.60	252.2962	H	19.23	0.33	10	0.11	26.37
Ab-16	TEH-(-3.7m)	Changhsingian	*C. nodosa*	-3.70	252.3131	C	19.83	0.33	13	0.09	23.67
Ab-17	TEH-(-3.9m)	Changhsingian	*C. bachmanni*	-3.90	252.3470	C	19.63	0.18	8	0.06	24.59
Ab-18	TEH-(-4.0 ~ -4.13m)	Changhsingian	*C. bachmanni*	-4.05	252.3723	C	19.24	0.31	9	0.10	26.33
Ab-19	TEH-(-4.25 ~ -4.3m)	Changhsingian	*C. bachmanni*	-4.28	252.4112	C	19.74	0.16	10	0.05	24.07
Ab-20	TEH-(-4.5 ~ -4.55m)	Changhsingian	*C. bachmanni*	-4.52	252.4518	C	19.32	0.21	13	0.06	25.96
Ab-21	TEH-(-4.75 ~ -4.76m)	Changhsingian	*C. changxingensis*	-4.75	252.4908	C	19.81	0.33	10	0.10	23.74
Ab-22	TEH-(-4.75 ~ -4.76m)	Changhsingian	*C. changxingensis*	-4.75	252.4908	H	19.40	0.25	9	0.08	25.62
Ab-23	TEH-(-5.0 ~ -5.1m)	Changhsingian	*C. changxingensis*	-5.05	252.5415	C	19.79	0.27	14	0.07	23.86
Ab-24	TEH-(-5.5m)	Changhsingian	*C. changxingensis*	-5.50	252.6176	C	19.62	0.31	14	0.08	24.61
Ab-25	TEH-(-5.75m)	Changhsingian	*C. changxingensis*	-5.75	252.6599	C	19.75	0.28	15	0.07	24.03
Ab-26	TEH-(-5.75m)	Changhsingian	*C. changxingensis*	-5.75	252.6599	H	19.63	0.33	5	0.15	24.56
Ab-27	TEH-(-5.9m)	Changhsingian	*C. changxingensis*	-5.90	252.6853	H	19.17	0.34	9	0.11	26.61
Ab-28	TEH-(-6.3 ~ -6.4m)	Changhsingian	*C. changxingensis*	-6.35	252.7614	C	19.21	0.32	10	0.10	26.45
Ab-29	TEH-(-6.3 ~ -6.4m)	Changhsingian	*C. changxingensis*	-6.35	252.7614	H	19.38	0.32	10	0.10	25.70
Ab-30	TEH-(-6.7 ~ -6.77m)	Changhsingian	*C. changxingensis*	-6.75	252.8291	C	20.00	0.27	13	0.07	22.88
Ab-31	TEH-(-7.2 ~ -7.3m)	Changhsingian	*C. changxingensis*	-7.25	252.9136	C	20.15	0.27	11	0.08	22.25
Ab-32	TEH-(-7.45 ~ -7.55m)	Changhsingian	*C. changxingensis*	-7.50	252.9559	C	19.75	0.30	8	0.11	24.03
Ab-33	TEH-(-8.23 ~ -8.3m)	Changhsingian	*C. subcarinata*	-8.25	253.0828	C	19.50	0.32	15	0.08	25.14
Ab-34	TEH-(-8.7 ~ -8.8m)	Changhsingian	*C. subcarinata*	-8.75	253.1674	C	19.36	0.30	15	0.08	25.79
Ab-35	TEH-(-9.4 ~ -9.5m)	Changhsingian	*C. subcarinata*	-9.45	253.2858	C	19.78	0.32	11	0.10	23.89
Ab-36	TEH-(-10 ~ -10.05m)	Changhsingian	*C. subcarinata*	-10.02	253.3822	C	19.52	0.27	12	0.08	25.07
Ab-37	TEH-(-10.4 ~ -10.5m)	Changhsingian	*C. subcarinata*	-10.45	253.4549	C	19.41	0.35	11	0.11	25.55
Ab-38	TEH-(-11.2 ~ -11.3m)	Changhsingian	*C. subcarinata*	-11.25	253.5903	C	18.95	0.24	8	0.09	27.62
Ab-39	TEH-(-11.95 ~ -12m)	Changhsingian	*C. subcarinata*	-11.98	253.7137	C	19.80	0.31	12	0.09	23.81
Ab-40	TEH-(-12.45 ~ -12.5m)	Changhsingian	*C. subcarinata*	-12.48	253.7983	C	19.86	0.29	9	0.10	23.55
Ab-41	TEH-(-14.15 ~ -14.2m)	Changhsingian	*C. wangi*	-14.18	254.0859	C	19.64	0.31	12	0.09	24.53
Ab-42	TEH-(-14.9 ~ -15m)	Wuchiapingian	*C. orientails*	-14.95	254.2098	C	19.16	0.23	6	0.10	26.69
Ab-43	TEH-(-16m)	Wuchiapingian	*C. orientails*	-16.00	254.3725	C	19.53	0.31	11	0.09	25.02
Ab-44	TEH-(-17m)	Wuchiapingian	*C. orientails*	-17.00	254.5275	C	19.63	0.30	11	0.09	24.56
Ab-45	TEH-(-18m)	Wuchiapingian	*C. orientails*	-18.00	254.6825	C	19.33	0.33	12	0.09	25.93
Ab-46	TEH-(-19m)	Wuchiapingian	*C. orientails*	-19.00	254.8375	C	19.52	0.22	8	0.08	25.04
Ab-47	TEH-(-19.4m)	Wuchiapingian	*C. orientails*	-19.40	254.8995	C	19.24	0.24	10	0.08	26.34
Ab-48	TEH-(-19.4m)	Wuchiapingian	*C. orientails*	-19.40	254.8995	H	18.64	0.27	10	0.08	29.01
Ab-49	TEH-(-20 ~ -20.1m)	Wuchiapingian	*C. transcaucasica*	-20.05	255.0003	C	19.60	0.28	6	0.11	24.70
Ab-50	TEH-(-21.2m)	Wuchiapingian	*C. transcaucasica*	-21.20	255.1785	C	18.85	0.34	11	0.10	28.09
Ab-51	TEH-(-21.9 ~ -22m)	Wuchiapingian	*C. transcaucasica*	-21.95	255.2948	C	19.32	0.19	6	0.08	25.95
Ab-52	TEH-(-23.8m)	Wuchiapingian	*C. transcaucasica*	-23.80	255.5815	C	19.70	0.28	6	0.12	24.27
Ab-53	TEH-(-23.8m)	Wuchiapingian	*C. transcaucasica*	-23.80	255.5815	H	19.32	0.30	8	0.11	25.95
Ab-54	TEH-(-24.8m)	Wuchiapingian	*C. transcaucasica*	-24.80	255.7365	C	19.63	0.13	7	0.05	24.55
Ab-55	TEH-(-26m)	Wuchiapingian	*C. guangyuanensis*	-26.00	255.9225	C	19.07	0.16	2	0.11	27.08
Ab-56	TEH-(-27m)	Wuchiapingian	*C. guangyuanensis*	-27.00	256.0775	C	19.81	0.15	9	0.05	23.74
Ab-57	TEH-(-27m)	Wuchiapingian	*C. guangyuanensis*	-27.00	256.0775	H	19.48	0.26	8	0.09	25.25
Ab-58	TEH-(-28m)	Wuchiapingian	*C. guangyuanensis*	-28.00	256.2325	C	19.38	0.25	12	0.07	25.69
Ab-59	TEH-(-28.9m)	Wuchiapingian	*C. guangyuanensis*	-28.90	256.3720	C	19.64	0.23	7	0.09	24.52
Ab-60	TEH-(-30m)	Wuchiapingian	*C. guangyuanensis*	-30.00	256.5425	C	19.07	0.03	4	0.01	27.08
Ab-61	TEH-(-30m)	Wuchiapingian	*C. guangyuanensis*	-30.00	256.5425	H	18.82	0.23	4	0.11	28.22
Ab-62	TEH-(-31.6 ~ -31.7m)	Wuchiapingian	*C. leveni*	-31.65	256.7983	C	19.91	0.28	9	0.09	23.32
Ab-63	TEH-(-31.6 ~ -31.7m)	Wuchiapingian	*C. leveni*	-31.65	256.7983	H	18.98	0.23	4	0.12	27.50
Ab-64	TEH-(-32.2 ~ -32.3m)	Wuchiapingian	*C. leveni*	-32.25	256.8913	C	19.48	0.25	5	0.11	25.22
Ab-65	TEH-(-32.2 ~ -32.3m)	Wuchiapingian	*C. leveni*	-32.25	256.8913	H	19.71	0.31	2	0.22	24.23
Ab-66	TEH-(-34.3 ~ -34.4m)	Wuchiapingian	*C. leveni*	-34.35	257.2168	H	19.60	0.22	7	0.08	24.72
Ab-67	TEH-(-36m)	Wuchiapingian	*C. asymmetrica*	-36.00	257.4725	H	19.47	0.23	8	0.08	25.30
Ab-68	TEH-(-36m)	Wuchiapingian	*C. asymmetrica*	-36.00	257.4725	R	18.86	0.23	5	0.10	28.04
Ab-69	TEH-(-36.2m)	Wuchiapingian	*C. asymmetrica*	-36.20	257.5035	H	19.33	0.28	8	0.10	25.91
Ab-70	TEH-(-36.6 ~ -36.68m)	Wuchiapingian	*C. asymmetrica*	-36.65	257.5733	H	19.48	0.32	8	0.11	25.26
Ab-71	TEH-(-38.5 ~ -38.6m)	Wuchiapingian	*C. asymmetrica*	-38.55	257.8678	C	18.28	0.22	9	0.07	30.66
Ab-72	TEH-(-42 ~ -42.1m)	Wuchiapingian	*C. dukouensis*	-42.05	258.4103	C	19.27	0.23	5	0.10	26.16

1 – R = ramiform; H = *Hindeodus* sp.; C = *Clarkina* sp.

2 – sd = Standard deviation of replicate analyses for each sample.

3 – se = Standard error of mean of replicate analyses for each sample.

4 – T(°C) = calculated seawater temperatures based on the equation of Lécuyer et al. (2013)

the density of sampling, quantity of recovered conodont elements, and temporal controls by U-Pb geochronology and/or conodont biostratigraphy varies from section to section, slight differences regarding the timing of magnitude of this substantial decrease in $\delta^{18}O_{apatite}$ do exist. Because the in situ SIMS method is fundamentally different from the conventional IRMS technique (Chen et al., 2016), we herein only compare the SIMS datasets (Table 3). By this comparison, the magnitude of climate warming ranges from 8.8 to 10.7 °C, with the highest temperature increase documented at the Penglaitan (Shen et al., 2019b) section and the lowest recorded at the Daijiagou section (Chen et al., 2016). As for the timing, although the starting and ending points vary from section to section (potentially due to insufficient sampling at certain sections; Table 3), the main phases of the climate warming (i.e., $\delta^{18}O_{apatite}$ values changing from high to low) occur in the interval of *C. meishanensis* (standard zone in South China, equivalent to *C. abadehensis* and *C. hauschkei* zones in Iran; Shen and Mei, 2010) – *H. changxingensis* – *H. praeparvus* zones, which is above the mass extinction horizon, within the maximum duration of the EPME (Shen et al., 2011, 2019b; Chen et al., 2016) and below the PTB.

In summary, oxygen isotopic compositions measured by high-resolution in situ SIMS and conventional IRMS methods on conodont apatite from Iran, Armenia, and South China (Korte et al., 2004; Joachimski et al., 2012, 2020; Sun et al., 2012; Chen et al., 2013; Schobben et al., 2014; Jiang et al., 2015; Chen et al., 2016; Shen et al., 2019b; Wang et al., 2020; this study) demonstrate highly comparable patterns indicating an abrupt decrease (~2‰, VSMOW) above the mass extinction horizon and a correspondingly rapid climate warming (~10 °C) in the latest Permian, which can be regarded as a global signature.

5.2. No cooling around the Wuchiapingian-Changhsingian boundary in Iran

A composite, long-term trend of oxygen isotopic compositions measured on conodont apatite, mainly reconstructed based on archives from the Permian-earliest Triassic in South China (Chen et al., 2013), suggested a substantial increase by ~2‰ starting from the early Wuchiapingian and lasting until the late Changhsingian. This could potentially translate into a climate cooling of ~9 °C. A segment of this increase in $\delta^{18}O_{apatite}$ was documented at the Meishan GSSP section (Chen et al., 2016). With better temporal controls from conodont

biostratigraphy and U-Pb geochronology, high-resolution SIMS data from Meishan show that $\delta^{18}O_{apatite}$ values increase from 19.2‰ immediately above the WCB (0.19 m above the base of *Clarkina wangi* Zone) to 21.0‰ at 1.71 m above the WCB, which suggests a drop of ~8 °C within 0.2 Ma (Chen et al., 2016). The fact that $\delta^{18}O_{apatite}$ values for most of the Changhsingian are on average higher than in the Wuchiapingian by ~2‰ is also evident in the Xikou (Wang et al., 2020) and Shangsi (unpublished data of J. Chen) sections.

In contrast, no substantial increase of $\delta^{18}O_{apatite}$ values measured with IRMS method has been reported from the corresponding lower Wuchiapingian-upper Changhsingian interval in the Iranian (Korte et al., 2004; Chen et al., 2013; Schobben et al., 2014) and Armenian (Joachimski et al., 2020) sections in the Neotethys region. Our high-resolution SIMS record from Abadeh further strengthens this conclusion, as shown in the compilation of the Iranian data (Figs. 3, 4). It is worth noting that, since $\delta^{18}O$ value of the standard NBS 120c was reported as 22.4‰ VSMOW in Korte et al. (2004) and 22.48‰ VSMOW in Chen et al. (2013), respectively, for the purpose of comparison, corrections need to be made on those two datasets (Korte et al., 2004; Chen et al., 2013) to accord with the newly recommended value of 21.7‰ VSMOW (Chen et al., 2016; Joachimski et al., 2020), as reported in Schobben et al. (2014). It is now clear that, during most the Lopingian and prior to the latest Permian abrupt decrease, $\delta^{18}O_{apatite}$ values are relatively stable and fluctuate around 19.5‰ with a variation only ~1‰, if excluding some rare "abnormal" data points (Figs. 3, 4). In short, climate cooling around the WCB is absent in Iran.

5.3. Siberian Traps magmatism and its palaeoenvironmental impact

Using the constraining data of the Abadeh section as listed in Table 1, sediment accumulation rates are calculated for each interval, and numeric age estimates are allocated for each sample/data point (Table 2). Subsequently, a high-precision temporal framework can be established at Abadeh, and the results (Fig. 3C) as well as the comparison with Meishan record (Fig. 4) can be evaluated from a temporal perspective. Assuming that the oxygen isotopic compositions of seawater at Abadeh and Meishan were the same (-1‰ VSMOW), calculated seawater temperatures remain relatively low at the mass extinction horizon (251.941 Ma) in Abadeh as well as at Meishan, with the
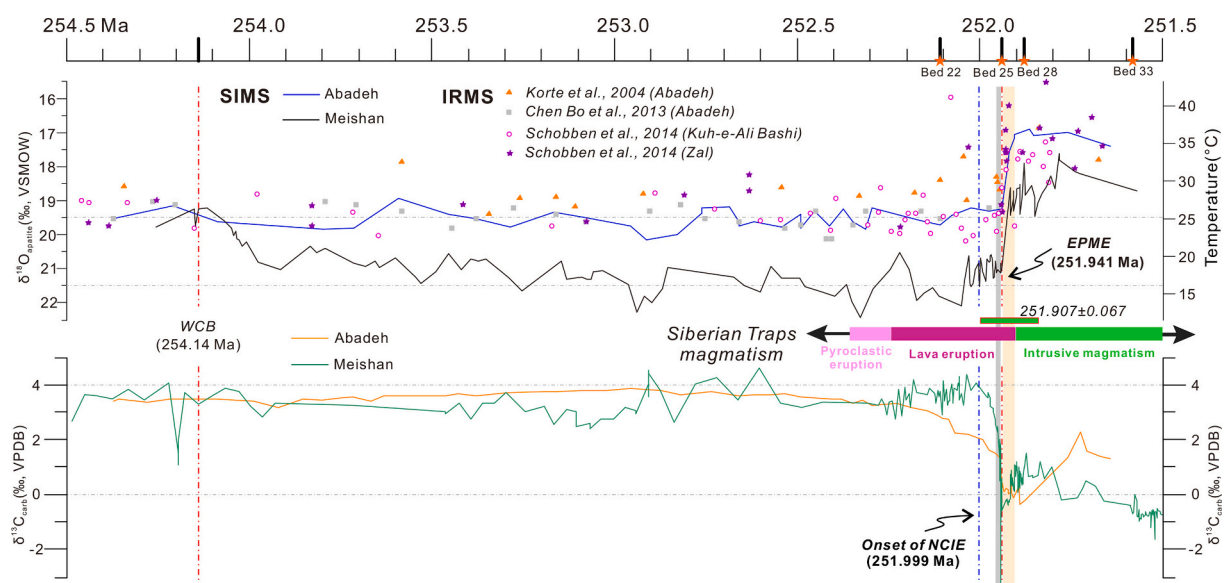

Fig. 4. The $\delta^{18}O_{apatite}$ profiles from Meishan, South China (Chen et al., 2016) and Abadeh, central Iran (this study) that are obtained from in situ SIMS method, as well as previously published $\delta^{18}O_{apatite}$ records from Iran (Korte et al., 2004; Chen et al., 2013; Schobben et al., 2014) that are measured with conventional IRMS technique, $\delta^{13}C_{carb}$ trends at the Meishan (Burgess et al., 2014; Chen et al., 2016) and Abadeh (Liu et al., 2013) sections, and the history of the Siberian Traps magmatism (including explosive, effusive, and intrusive phases) (Burgess and Bowring, 2015), all of which are projected onto a unified temporal framework.

Table 3

A comparison of timing and magnitude of climate warming documented in seven sections in South China (Chen et al., 2016; Shen et al., 2019b; Wang et al., 2020) and Iran (this study), all of which are based on high-resolution in situ SIMS method.

Section	Before					After					ΔT(°C)
	$\delta^{18}O_{apatite}$	1σ	Temp.	Sample	Cododont zone	$\delta^{18}O_{apatite}$	1σ	Temp.	Sample	Cododont zone	
Meishan	21.00	0.27	18.4	MS 25	*C. meishanensis*	18.64	0.36	29.0	MS 27-1	*H. changxingensis-H. praeparvus*	10.6
Shangsi	20.78	0.26	19.4	SHS-(99.92-100.05m)	*C. meishanensis*	18.46	0.23	29.8	SHS-(100.4-100.5m)	*H. eurypyge*	10.4
Daijiagou	19.59	0.28	24.8	DJG-(0.15 ~ 0.2m)	*C.yini*	17.62	0.23	33.6	DJG-(0.61 ~ 0.69m)	*H. changxingensis-H. praeparvus*	8.8
Liangfengya	19.41	0.21	25.5	LFY-30	*C. yini*	17.18	0.34	35.6	LFY-34-Upper	*H. praeparvus*	10.1
Penglaitan	17.86	0.25	32.5	HSH-PT 2.1m	*C. meishanensis-H. praeparvus*	15.50	0.26	43.2	PLT09-C-63.32-63.35m	*H. parvus*	10.7
Xikou	20.87	0.02	18.9	XK-3316 m	*C. yini*	18.68	0.42	28.8	XK-3317.6 m	*H. praeparvus*	9.9
Abadeh	19.26	0.27	26.2	TEH-(-1.5m)	*C. hauschkei*	17.05	0.24	36.2	TEH-(-0.06m)	*C. hauschkei*	10.0

value of 26.2 °C and 18.4 °C, respectively. Above the mass extinction horizon, seawater temperatures rise to 36.2 °C at 251.904 Ma and 29.0 °C at 251.918 Ma in Abadeh and Meishan, respectively. In other words, it took a maximum duration of ~37 kyr for warming of 10.0 °C at Abadeh, and ~23 kyr for warming of 10.6 °C at Meishan (Table 3). As shown in the highly expanded Penglaitan section, the duration is even much shorter and likely took only about several thousand years (Shen et al., 2019b). Such rates of global warming in Earth history are undoubtedly rapid by geological measures, and often considered to be potentially associated with major LIP events (Ernst and Youbi, 2017).

The Siberian Traps magmatism represents one of the most voluminous continental flood basalt (CFB) events in the Phanerozoic (Reichow et al., 2009; Ernst, 2014; Ernst and Youbi, 2017). A conservative estimate (Reichow et al., 2009; Saunders and Reichow, 2009) suggested 5 × 10^6 km^2 and 3 × 10^6 km^3 for the size and volume, respectively, whereas Ivanov (2007) estimated these two criteria could be higher as about 7 × 10^6 km^2 and 4 × 10^6 km^3. In either case, the Siberian Traps can be classified as major LIP (i.e., with a size in the range of 1-10 × 10^6 km^3), among the ranks of CAMP (Central Atlantic Magmatic Province) and Karoo-Ferrar LIPs (Ernst, 2014). Using high-precision CA-TIMS (chemical-abrasion thermal ionization mass spectrometry) dating technique, Burgess and Bowring (2015) presented an updated, more precise and complete timeline for the history of the Siberian Traps magmatism (Fig. 4):

(1) Stage 1, beginning just prior to 252.24 ± 0.12 Ma, was characterized by initial pyroclastic eruptions followed by lava effusion. During this stage, an estimated 2/3 of the total volume of Siberian Traps lavas was emplaced (> 1 × 10^6 km^3).
(2) Stage 2, beginning at 251.907 ± 0.067 Ma and ending at 251.483 ± 0.088 Ma, was characterized by cessation of extrusive magmatism and widespread sill intrusions.
(3) Lava eruptions resumed at 251.483 ± 0.088 Ma after a hiatus of ~420 kyr, marking the beginning of Stage 3. The end of Stage 3 was estimated at 250.2 ± 0.3 Ma, based on baddeleyite extracted from carbonatite in the Guli complex (Kamo et al., 2003).

According to the high-precision age model from Burgess and Bowring (2015), in which they suggested that two-thirds of the total pyroclastic/lava volume of 4 × 10^6 km^3 of the Siberian Traps was erupted in ~300 kyr, a volcanic flux (i.e., eruption rate) of 8.9 km^3/yr can be calculated (Chen and Xu, 2019). In addition, another critical attribute of the Siberian Traps magmatism is its enormous gas production (Svensen et al., 2009; Sobolev et al., 2011; Black et al., 2012; Broadley et al., 2018). This aspect is pivotal especially related to recycled oceanic crust (Sobolev et al., 2011), infiltration of subducted seawater-derived volatiles (Broadley et al., 2018), and sill intrusions and contact metamorphism when ascending magma interacted

predominantly with evaporites, carbonates, and organic-rich sediments (Svensen et al., 2009; Polozov et al., 2016; Burgess et al., 2017; Black et al., 2018; Svensen et al., 2018). Therefore, a combination of high volcanic flux and gas production of the Siberian Traps magmatism enabled it to be annihilating to profoundly affect the biosphere, atmosphere, and hydrosphere.

In this study, we project the carbonate carbon isotopes ($\delta^{13}C_{carb}$), oxygen isotopes of conodont apatite ($\delta^{18}O_{apatite}$), the tempo of the mass extinction at the Abadeh and Meishan sections, and the temporal evolution of the Siberian Traps magmatism (including explosive, effusive, and intrusive phases) onto a unified timescale (Fig. 4). Although the bulk-rock $\delta^{13}C_{carb}$ trend slightly varies among the investigated sections such as in Iran and South China (Korte and Kozur, 2010; Shen et al., 2013; Schobben et al., 2017), a first-order global trend towards depleted values can still be recognized (Schobben et al., 2017). From a global perspective, the majority of these negative carbon isotope excursions (NCIE) covers the biostratigraphic interval from the *Clarkina yini* to the *Hindeodus parvus* zones (Schobben et al., 2017; Henderson, 2018), corresponding to 252.046 to 251.880 Ma based on the temporal framework of the Meishan GSSP section (Chen et al., 2016). Climate warming obviously postdated the onset of NCIE by at least ~81 kyr at Meishan (Chen et al., 2016) and ~288 kyr at Abadeh (Figs. 3, 4), although both occurred during a restricted interval of the Siberian Traps magmatism (Fig. 4). If we consider the uncertainties in the U-Pb ages (Burgess and Bowring, 2015) and our age estimates based on constrained data and sediment accumulation rates (Chen et al., 2016; Table 1 of this study), the rapid declines in $\delta^{13}C_{carb}$ (i.e., carbon cycle disruption) and $\delta^{18}O_{apatite}$ (i.e., climate warming) coincide with the switch from dominantly extrusive eruptions to widespread sill intrusions of the Siberian Traps magmatism (Fig. 4). The temporal relationships between changes in $\delta^{13}C_{carb}$ and $\delta^{18}O_{apatite}$, and different phases of the Siberian Traps magmatism are difficult to explain and await further comprehensive studies such as climate modeling. At the moment, we propose that early pyroclastic and lava eruptions did not initiate immediate substantial responses in the global carbon cycle and seawater temperatures. After protracted degassing of CO_2 and CH_4 among other types of volatiles, a tipping point was reached around 252.229 Ma at Abadeh and 251.999 at Meishan when the disruption of carbon cycle began. Around 251.907 ± 0.067 Ma (Burgess and Bowring, 2015; Burgess et al., 2017), the emplacement style of the Siberian Traps magmatism switched from dominantly extrusive lava eruptions to widespread sill intrusions. The vast Tunguska Basin contains thick deposits of evaporites, carbonates, and organic-rich shales of Cambrian to Permian age (Svensen et al., 2009; Svensen et al., 2018). Widespread magmatic intrusions and associated contact metamorphism have much profound impact than magma degassing alone, as indicated in a recent thermal modeling study (Svensen et al., 2018). Therefore, the aforementioned switch is probably the most annihilating phase of

the Siberian Traps magmatism and potentially the last straw causing global environmental deterioration and ultimately the end-Permian mass extinction.

6. Conclusions

Measured with in situ SIMS method, oxygen isotopic compositions of conodont apatite ($\delta^{18}O_{apatite}$) from the Abadeh section in central Iran provide a continuous, high-resolution relative seawater temperature record during the Late Permian-earliest Triassic in the Neotethys. The seawater temperatures were largely stable with only limited fluctuations during most of the Wuchiapingian and Changhsingian, indicating that previously documented climate cooling around the Wuchiapingian-Changhsingian boundary in South China (e.g., Meishan, Shangsi) is probably only a local or regional event. An abrupt warming with a magnitude of ~10 °C (i.e., a decrease of ~2‰ in $\delta^{18}O_{apatite}$) occurs in the lowest part of Unit a (Elikah Formation), or to be precise, in the *Clarkina hauschkei* Zone of the uppermost Permian, above the mass extinction horizon and below the Permian-Triassic boundary. Moreover, the Abadeh record is consistent with previous results documented in South China, Iran, and Armenia in terms of the timing and magnitude of a substantial warming in the latest Permian, and therefore represents a global signature. Based on correlation with the Meishan GSSP section, we estimate that the abrupt warming of ~10 °C at Abadeh happened between 251.941 and 251.904 Ma, and took only a maximum duration of ~37 kyr. More significantly, such as temperature rise coincides with the switch from dominantly extrusive eruptions to widespread sill intrusions of the Siberian Traps magmatism. This suggests release of substantial crustal carbon probably triggered by magmatic intrusion, which caused substantial environmental and biological changes in the latest Permian and led to the end-Permian mass extinction.

Supplementary data to this article can be found online at https://doi.org/10.1016/j.palaeo.2020.109973.

Declaration of Competing Interest

The authors declare that they have no conflict of interests to this work.

References

Algeo, T.J., Chen, Z.Q., Fraiser, M.L., Twitchett, R.J., 2011. Terrestrial-marine teleconnections in the collapse and rebuilding of Early Triassic marine ecosystems. Palaeogeogr. Palaeoclimatol. Palaeoecol. 308, 1–11.

Angiolini, L., Crippa, G., Shen, S.Z., Zhang, H., Zhang, Y.C., Ghorbani, M., Ghorbani, M., Ovissi, M., 2017. Report of the Chinese, Italian, Iranian working group: The Permian-Triassic boundary sections of Abadeh revisited. Permophiles 65, 24–27.

Black, B.A., Elkins-Tanton, L.T., Rowe, M.C., Peate, I.U., 2012. Magnitude and consequences of volatile release from the Siberian Traps. Earth Planet. Sci. Lett. 317, 363–373.

Black, B.A., Neely, R.R., Lamarque, J.-F., Elkins-Tanton, L.T., Kiehl, J.T., Shields, C.A., Mills, M.J., Bardeen, C., 2018. Systemic swings in end-Permian climate from Siberian Traps carbon and sulfur outgassing. Nat. Geosci. 11, 949–954.

Bond, D.P.G., Grasby, S.E., 2017. On the causes of mass extinctions. Palaeogeogr. Palaeoclimatol. Palaeoecol. 478, 3–29.

Bond, D.P.G., Wignall, P.B., 2014. Large igneous provinces and mass extinctions: An update. In: Keller, G., Kerr, A.C. (Eds.), Volcanism, Impacts, and Mass Extinctions: Causes and Effects. 505. Geological Society of America Special Paper, pp. 29–55.

Broadley, M.W., Barry, P.H., Ballentine, C.J., Taylor, L.A., Burgess, R., 2018. End-Permian extinction amplified by plume-induced release of recycled lithospheric volatiles. Nat. Geosci. 11, 682–687.

Burgess, S.D., Bowring, S.A., 2015. High-precision geochronology confirms voluminous magmatism before, during, and after Earth's most severe extinction. Sci. Adv. 1, e1500470.

Burgess, S.D., Bowring, S.A., Shen, S.Z., 2014. High-precision timeline for Earth's most severe extinction. Proc. Natl. Acad. Sci. 111, 3316–3321.

Burgess, S.D., Muirhead, J.D., Bowring, S.A., 2017. Initial pulse of Siberian Traps sills as the trigger of the end-Permian mass extinction. Nat. Commun. 8, 164.

Chen, B., Joachimski, M.M., Shen, S.Z., Lambert, L.L., Lai, X.L., Wang, X.D., Chen, J., Yuan, D.X., 2013. Permian ice volume and palaeoclimate history: Oxygen isotope proxies revisited. Gondwana Res. 24, 77–89.

Chen, J., Xu, Y.G., 2019. Establishing the link between Permian volcanism and biodiversity changes: Insights from geochemical proxies. Gondwana Res. 75, 68–96.

Chen, J., Beatty, T.W., Henderson, C.M., Rowe, H., 2009. Conodont biostratigraphy across the Permian–Triassic boundary at the Dawen section, Great Bank of Guizhou, Guizhou Province, South China: Implications for the Late Permian extinction and correlation with Meishan. J. Asian Earth Sci. 36, 442–458.

Chen, J., Shen, S.Z., Li, X.H., Xu, Y.G., Joachimski, M.M., Bowring, S.A., Erwin, D.H., Yuan, D.X., Chen, B., Zhang, H., Wang, Y., Cao, C.Q., Zheng, Q.F., Mu, L., 2016. High-resolution SIMS oxygen isotope analysis on conodont apatite from South China and implications for the end-Permian mass extinction. Palaeogeogr. Palaeoclimatol. Palaeoecol. 448, 26–38.

Courtillot, V.E., Renne, P.R., 2003. On the ages of flood basalt events. Compt. Rendus Geosci. 335, 113–140.

Dessert, C., Dupre, B., Gaillardet, J., Francois, L.M., Allegre, C.J., 2003. Basalt weathering laws and the impact of basalt weathering on the global carbon cycle. Chem. Geol. 202, 257–273.

Ernst, R.E., 2014. Large Igneous Provinces. Cambridge University Press, Cambridge, UK.

Ernst, R.E., Youbi, N., 2017. How Large Igneous Provinces affect global climate, sometimes cause mass extinctions, and represent natural markers in the geological record. Palaeogeogr. Palaeoclimatol. Palaeoecol. 478, 30–52.

Ganino, C., Arndt, N.T., 2009. Climate changes caused by degassing of sediments during the emplacement of large igneous provinces. Geology 37, 323–326.

Ghaderi, A., Garbelli, C., Angiolini, L., Ashouri, A.R., Korn, D., Rettori, R., Gharaie, M.H.M., 2014a. Faunal change near the end-Permian extinction: the brachiopods of the Ali Bashi Mountains, NW Iran. Riv. Ital. Paleontol. Stratigr. 120, 27–59.

Ghaderi, A., Leda, L., Schobben, M., Korn, D., Ashouri, A.R., 2014b. High-resolution stratigraphy of the Changhsingian (Late Permian) successions of NW Iran and the Transcaucasus based on lithological features, conodonts and ammonoids. Fossil Record 17, 41–57.

Gliwa, J., Ghaderi, A., Leda, L., Schobben, M., Tomás, S., Foster, W.J., Forel, M.B., Ghanizadeh Tabrizi, N., Grasby, S.E., Struck, U., Ashouri, A.R., Korn, D., 2020. Aras Valley (northwest Iran): high-resolution stratigraphy of a continuous central Tethyan Permian–Triassic boundary section. Fossil Record 23, 33–69.

Grard, A., Francois, L.M., Dessert, C., Dupre, B., Godderis, Y., 2005. Basaltic volcanism and mass extinction at the Permo-Triassic boundary: Environmental impact and modeling of the global carbon cycle. Earth Planet. Sci. Lett. 234, 207–221.

Hassanzadeh, J., Wernicke, B.P., 2016. The Neotethyan Sanandaj-Sirjan zone of Iran as an archetype for passive margin-arc transitions. Tectonics 35, 586–621.

Henderson, C.M., 2018. Permian conodont biostratigraphy, In: Lucas, S.G., Shen, S.Z. (Eds.), The Permian Timescale. Geol. Soc. Lond., Spec. Publ. 450, 119–142.

Heydari, E., Hassandzadeh, J., Wade, W.J., 2000. Geochemistry of central Tethyan Upper Permian and Lower Triassic strata, Abadeh region, Iran. Sediment. Geol. 137, 85–99.

Heydari, E., Hassanzadeh, J., Wade, W.J., Ghazi, A.M., 2003. Permian-Triassic boundary interval in the Abadeh section of Iran with implications for mass extinction: Part 1-Sedimentology. Palaeogeogr. Palaeoclimatol. Palaeoecol. 193, 405–423.

Horacek, M., Richoz, S., Brandner, R., Krystyn, L., Spötl, C., 2007. Evidence for recurrent changes in Lower Triassic oceanic circulation of the Tethys: The δ13C record from marine sections in Iran. Palaeogeogr. Palaeoclimatol. Palaeoecol. 252, 355–369.

Ivanov, A.V., 2007. Evaluation of different models for the origin of the Siberian Traps. Plates, Plumes and Planetary Processes 430, 669–689.

Jiang, H.S., Joachimski, M.M., Wignall, P.B., Zhang, M.H., Lai, X.L., 2015. A delayed end-Permian extinction in deep-water locations and its relationship to temperature trends (Bianyang, Guizhou Province, South China). Palaeogeogr. Palaeoclimatol. Palaeoecol. 440, 690–695.

Jin, Y.G., Wang, Y., Henderson, C., Wardlaw, B.R., Shen, S.Z., Cao, C.Q., 2006. The Global Boundary Stratotype Section and Point (GSSP) for the base of Changhsingian Stage (Upper Permian). Episodes 29, 175–182.

Joachimski, M.M., Breisig, S., Buggisch, W., Talent, J.A., Mawson, R., Gereke, M., Morrow, J.R., Day, J., Weddige, K., 2009. Devonian climate and reef evolution:

Insights from oxygen isotopes in apatite. Earth Planet. Sci. Lett. 284, 599–609.

Joachimski, M.M., Lai, X.L., Shen, S.Z., Jiang, H.S., Luo, G.M., Chen, B., Chen, J., Sun, Y.D., 2012. Climate warming in the latest Permian and the Permian–Triassic mass extinction. Geology 40, 195–198.

Joachimski, M.M., Alekseev, A.S., Grigoryan, A., Gatovsky, Y.A., 2020. Siberian Trap volcanism, global warming and the Permian-Triassic mass extinction: New insights from Armenian Permian-Triassic sections. Geol. Soc. Am. Bull. 132, 427–443.

Johansson, L., Zahirovic, S., Müller, R.D., 2018. The interplay between the eruption and weathering of Large Igneous Provinces and the deep-time carbon cycle. Geophys. Res. Lett. 45, 5380–5389.

Kamo, S.L., Czamanske, G.K., Amelin, Y., Fedorenko, V.A., Davis, D.W., Trofimov, V.R., 2003. Rapid eruption of Siberian flood-volcanic rocks and evidence for coincidence with the Permian-Triassic boundary and mass extinction at 251 Ma. Earth Planet. Sci. Lett. 214, 75–91.

Kershaw, S., Crasquin, S., Li, Y., Collin, P.Y., Forel, M.B., Mu, X., Baud, A., Wang, Y., Xie, S., Maurer, F., Guo, L., 2012. Microbialites and global environmental change across the Permian-Triassic boundary: a synthesis. Geobiology 10, 25–47.

Korn, D., Ghaderi, A., Leda, L., Schobben, M., Ashouri, A.R., 2016. The ammonoids from the Late Permian Paratirolites Limestone of Julfa (East Azerbaijan, Iran). J. Syst. Palaeontol. 14, 841–890.

Korte, C., Kozur, H.W., 2010. Carbon-isotope stratigraphy across the Permian-Triassic boundary: A review. J. Asian Earth Sci. 39, 215–235.

Korte, C., Kozur, H.W., Joachimski, M.M., Strauss, H., Veizer, J., Schwark, L., 2004. Carbon, sulfur, oxygen and strontium isotope records, organic geochemistry and biostratigraphy across the Permian/Triassic boundary in Abadeh, Iran. Int. J. Earth Sci. 93, 565–581.

Kozur, H.W., 2004. Pelagic uppermost Permian and the Permian-Triassic boundary conodonts of Iran. Part I: Taxonomy. Hallesches Jahrbuch für Geowissenschaften B Beiheft 18, 39–68.

Kozur, H.W., 2005. Pelagic uppermost Permian and the Permian-Triassic boundary conodonts of Iran. Part II: investigated sections and evaluation of the conodont faunas. Hallesches Jahrbuch für Geowissenschaften B Beiheft 19, 49–86.

Kozur, H.W., 2007. Biostratigraphy and event stratigraphy in Iran around the Permian-Triassic Boundary (PTB): Implications for the causes of the PTB biotic crisis. Glob. Planet. Chang. 55, 155–176.

Lécuyer, C., Amiot, R., Touzeau, A., Trotter, J., 2013. Calibration of the phosphate d^{18}O thermometer with carbonate-water oxygen isotope fractionation equations. Chem. Geol. 347, 217–226.

Leda, L., Korn, D., Ghaderi, A., Hairapetian, V., Struck, U., Reimold, W.U., 2014. Lithostratigraphy and carbonate microfacies across the Permian–Triassic boundary near Julfa (NW Iran) and in the Baghuk Mountains (Central Iran). Facies 60, 295–325.

Li, X.H., Li, W.X., Li, Q.L., Wang, X.C., Liu, Y., Yang, Y.H., 2010a. Petrogenesis and tectonic significance of the ~850 Ma Gangbian alkaline complex in South China: Evidence from in situ zircon U–Pb dating, Hf–O isotopes and whole-rock geochemistry. Lithos 114, 1–15.

Li, X.H., Long, W.G., Li, Q.L., Liu, Y., Zheng, Y.F., Yang, Y.H., Chamberlain, K.R., Wan, D.F., Guo, C.H., Wang, X.C., 2010b. Penglai zircon megacrysts: a potential new working reference material for microbeam determination of Hf–O isotopes and U–Pb age. Geostand. Geoanal. Res. 34, 117–134.

Liu, X.C., Wang, W., Shen, S.Z., Gorgij, M.N., Ye, F.C., Zhang, Y.C., Furuyama, S., Kano, A., Chen, X.Z., 2013. Late Guadalupian to Lopingian (Permian) carbon and strontium isotopic chemostratigraphy in the Abadeh section, central Iran. Gondwana Res. 24, 222–232.

Muttoni, G., Kent, D.V., 2019. Adria as promontory of Africa and its conceptual role in the Tethys Twist and Pangea B to Pangea A Transformation in the Permian. Riv. Ital. Paleontol. Stratigr. 125, 249–269.

Polozov, A.G., Svensen, H.H., Planke, S., Grishina, S.N., Fristad, K.E., Jerram, D.A., 2016. The basalt pipes of the Tunguska Basin (Siberia, Russia): High temperature processes and volatile degassing into the end-Permian atmosphere. Palaeogeogr. Palaeoclimatol. Palaeoecol. 441, 51–64.

Rampino, M.R., Stothers, R.B., 1988. Flood basalt volcanism during the past 250 million years. Science 241, 663–668.

Reichow, M.K., Pringle, M.S., Al'Mukhamedov, A.I., Allen, M.B., Andreichev, V.L., Buslov, M.M., Davies, C.E., Fedoseev, G.S., Fitton, J.G., Inger, S., Medvedev, A.Y., Mitchell, C., Puchkov, V.N., Safonova, I.Y., Scott, R.A., Saunders, A.D., 2009. The timing and extent of the eruption of the Siberian Traps large igneous province: Implications for the end-Permian environmental crisis. Earth Planet. Sci. Lett. 277, 9–20.

Renne, P.R., Basu, A.R., 1991. Rapid eruption of the Siberian Traps flood basalts at the Permo-Triassic boundary. Science 253, 176–179.

Renne, P.R., Zhang, Z.C., Richards, M.A., Black, M.T., Basu, A.R., 1995. Synchrony and causal relations between Permian-Triassic boundary crises and Siberian flood volcanism. Science 269, 1413–1416.

Richoz, S., Krystyn, L., Baud, A., Brandner, R., Horacek, M., Mohtat-Aghai, P., 2010. Permian-Triassic boundary interval in the Middle East (Iran and N. Oman): Progressive environmental change from detailed carbonate carbon isotope marine

curve and sedimentary evolution. J. Asian Earth Sci. 39, 236–253.

Robock, A., 2000. Volcanic eruptions and climate. Rev. Geophys. 38, 191–219.

Saltzman, M.R., 2017. Silicate weathering, volcanic degassing, and the climate tug of war. Geology 45, 763–764.

Saunders, A., Reichow, M., 2009. The Siberian Traps and the End-Permian mass extinction: a critical review. Chin. Sci. Bull. 54, 20–37.

Schobben, M., Joachimski, M.M., Korn, D., Leda, L., Korte, C., 2014. Palaeotethys seawater temperature rise and an intensified hydrological cycle following the end-Permian mass extinction. Gondwana Res. 26, 675–683.

Schobben, M., van de Velde, S., Gliwa, J., Leda, L., Korn, D., Struck, U., Ullmann, C.V., Hairapetian, V., Ghaderi, A., Korte, C., Newton, R.J., Poulton, S.W., Wignall, P.B., 2017. Latest Permian carbonate carbon isotope variability traces heterogeneous organic carbon accumulation and authigenic carbonate formation. Clim. Past 13, 1635–1659.

Shen, S.Z., Mei, S.L., 2010. Lopingian (Late Permian) high-resolution conodont biostratigraphy in Iran with comparison to South China zonation. Geol. J. 45, 135–161.

Shen, S.Z., Gorgij, M.N., Wang, W., Zhang, Y.C., Khamar, H.R., Tanatabaei, S.H., 2009. Report of field trip of the Permian stratigraphy in Central and Eastern Iran. Permophiles 53, 2–5.

Shen, S.Z., Crowley, J.L., Wang, Y., Bowring, S.A., Erwin, D.H., Sadler, P.M., Cao, C.Q., Rothman, D.H., Henderson, C.M., Ramezani, J., Zhang, H., Shen, Y.N., Wang, X.D., Wang, W., Mu, L., Li, W.Z., Tang, Y.G., Liu, X.L., Liu, L.J., Zeng, Y., Jiang, Y.F., Jin, Y.G., 2011. Calibrating the end-Permian mass extinction. Science 334, 1367–1372.

Shen, S.Z., Cao, C.Q., Zhang, H., Bowring, S.A., Henderson, C.M., Payne, J.L., Davydov, V.I., Chen, B., Yuan, D.X., Zhang, Y.C., Wang, W., Zheng, Q.F., 2013. High-resolution δ^{13}C$_{carb}$ chemostratigraphy from latest Guadalupian through earliest Triassic in South China and Iran. Earth Planet. Sci. Lett. 375, 156–165.

Shen, J., Yu, J., Chen, J., Algeo, T.J., Xu, G., Feng, Q., Shi, X., Planavsky, N.J., Shu, W., Xie, S., 2019a. Mercury evidence of intense volcanic effects on land during the Permian-Triassic transition. Geology 47, 1117–1121.

Shen, S.Z., Ramezani, J., Chen, J., Cao, C.Q., Erwin, D.H., Zhang, H., Xiang, L., Schoepfer, S.D., Henderson, C.M., Zheng, Q.F., Bowring, S.A., Wang, Y., Li, X.H., Wang, X.D., Yuan, D.X., Zhang, Y.C., Mu, L., Wang, J., Wu, Y.S., 2019b. A sudden end-Permian mass extinction in South China. Geol. Soc. Am. Bull. 131, 205–223.

Shooshtarizadeh, P., Yazdi, M., 2013. Conodont biostratigraphy of Permian-Triassic boundary deposits in Koh-e-Chan Kaland, North of Abadeh, Iran. Bulletin of the New Mexico Museum of Natural History and Science 61, 543–555.

Sobolev, S.V., Sobolev, A.V., Kuzmin, D.V., Krivolutskaya, N.A., Petrunin, A.G., Arndt, N.T., Radko, V.A., Vasiliev, Y.R., 2011. Linking mantle plumes, large igneous provinces and environmental catastrophes. Nature 477, 312–316.

Sun, Y.D., Joachimski, M.M., Wignall, P.B., Yan, C.B., Chen, Y.L., Jiang, H.S., Wang, L.N., Lai, X.L., 2012. Lethally hot temperatures during the Early Triassic greenhouse. Science 338, 366–370.

Svensen, H., Planke, S., Polozov, A.G., Schmidbauer, N., Corfu, F., Podladchikov, Y.Y., Jamtveit, B., 2009. Siberian gas venting and the end-Permian environmental crisis. Earth Planet. Sci. Lett. 277, 490–500.

Svensen, H.H., Frolov, S., Akhmanov, G.G., Polozov, A.G., Jerram, D.A., Shiganova, O.V., Melnikov, N.V., Iyer, K., Planke, S., 2018. Sills and gas generation in the Siberian Traps. Philos. Trans. R. Soc. A Math. Phys. Eng. Sci. 376, 20170080.

Taraz, H., 1969. Permo-Triassic section in central Iran. AAPG Bull. 53, 688–693.

Taraz, H., 1971. Uppermost Permian and Permo-Triassic transition beds in central Iran. AAPG Bull. 55, 1280–1294.

Taraz, H., 1973. Correlation of uppermost Permian in Iran, central Asia, and South China. AAPG Bull. 57, 1117–1133.

Taraz, H., 1974. Geology of the Surmag-Deh Bid area, Abadeh region, central Iran. Geol. Surv. Iran Rep. 37.

Taraz, H., Golshani, F., Nakazawa, K., Shimizu, D., Bando, Y., Ishii, K.-I., Murata, M., Okimura, Y., Sakagami, S., Nakamura, K., Tokuoka, T., 1981. The Permian and the Lower Triassic systems in Abadeh region, central Iran. Memoirs of the Faculty of Science, Kyoto University, Series of Geology and Mineralogy 47, 61–133.

Vennemann, T.W., Fricke, H.C., Blake, R.E., O'Neil, J.R., Colman, A., 2002. Oxygen isotope analysis of phosphates: A comparison of techniques for analysis of Ag$_3$PO$_4$. Chem. Geol. 185, 321–336.

Wang, W.Q., Garbelli, C., Zhang, F.F., Zheng, Q.F., Zhang, Y.C., Yuan, D.X., Shi, Y.K., Chen, B., Shen, S.Z., 2020. A high-resolution Middle to Late Permian paleotemperature curve reconstructed using oxygen isotopes of well-preserved brachiopod shells. Earth Planet. Sci. Lett.

Wang, X.D., Cawood, P.A., Zhao, H., Zhao, L.S., Grasby, S.E., Chen, Z.Q., Zhang, L., 2019. Global mercury cycle during the end-Permian mass extinction and subsequent Early Triassic recovery. Earth Planet. Sci. Lett. 513, 144–155.

Wignall, P.B., 2001. Large igneous provinces and mass extinctions. Earth Sci. Rev. 53, 1–33.

Zhong, Y.T., He, B., Mundil, R., Xu, Y.G., 2014. CA-TIMS zircon U-Pb dating of felsic ignimbrite from the Binchuan section: Implications for the termination age of Emeishan large igneous province. Lithos 204, 14–19.